Materials Advances

ROYAL SOCIETY OF CHEMISTRY

PAPER

View Article Online
View Journal | View Issue

Cite this: *Mater. Adv.*, 2024, 5, 5724

Adsorptive and photo-Fenton properties of bimetallic MIL-100(Fe,Sn) and MIL-100(Fe,Ir) MOFs toward removal of tetracycline from aqueous solutions†

Naghmeh Sadat Mirbagheri,[ab] Philipp A. Heizmann,[ab] Vanessa Trouillet,[cd] Jan Büttner,[aef] Anna Fischer[aef] and Severin Vierrath*[ab]

Bimetallic derivatives of MIL-100(Fe) are promising metal–organic frameworks (MOFs) that have caught increasing research and application attention in the last few years due to their superior potential compared to MIL-100(Fe) for treatment of wastewater. In this work, novel bimetallic MIL-100(Fe,Sn) and MIL-100(Fe,Ir) were synthesized using a facile synthesis method. The synthesized MOFs showed different activities toward removal of tetracycline (TC), a broad-spectrum antibiotic, from an aqueous solution under dark conditions, followed by photo-Fenton degradation. In this context, the best-performing Sn-doped MIL-100(Fe) MOFs, that is MIL-100(Fe,Sn-7.1), showed marginally increased adsorption and photo-Fenton activity compared to MIL-100(Fe), resulting in a TC removal efficiency of 76%. In contrast, the best-performing Ir-doped MIL-100(Fe), that is MIL-100(Fe,Ir-62.3), showed enhanced adsorption property by 34% compared to MIL-100(Fe), resulting in the best TC removal efficiency of 91% among the studied MOFs. The detailed analysis and characterization of the synthesized MOFs revealed that the average pore diameter of MIL-100(Fe,Ir-62.3) was approximately four times larger than that of MIL-100(Fe) and MIL-100(Fe,Sn-7.1), though they possessed the lowest surface area. This observation demonstrated that the pore size is an essential parameter to be considered in the process of adsorptive removal of TC from an aqueous solution, which led to the significantly enhanced overall efficiency of bimetallic MIL-100(Fe) derived MOFs.

Received 26th February 2024,
Accepted 2nd June 2024

DOI: 10.1039/d4ma00196f

rsc.li/materials-advances

Introduction

Nowadays, the amount of antibiotic consumption in agriculture and the health sector is growing rapidly.[1] Residual antibiotics can persist in water after disposal, posing a clear threat to ecosystems and raising the possibility of antibiotic resistance.[2] As reported by Robinson *et al.* in 2016,[3] antibiotic resistance has claimed the lives of approximately 700.000 individuals, and this number is expected to rise to ten million people by 2050. Therefore, numerous efforts have been made over the last decades to resolve this environmental issue.[4] In this context, heterogeneous photocatalysis, particularly in advanced oxidation processes, has been regarded as an efficient, low-cost and environmentally friendly technology for the treatment of antibiotic-contaminated water with the help of solar energy and hydroxyl radicals.[5]

MIL-100(Fe) is one of the well-known metal–organic frameworks (MOFs) that not only possess highly porous channels for heterogeneous photocatalysis but also are chemically active for advanced oxidation processes. In MIL-100(Fe) MOFs, the Fe_3-μ_3-oxo clusters harvest solar energy, creating charge separation, and producing highly reactive hydroxyl radicals in the presence of H_2O_2 *via* a photo-Fenton process, which can degrade released pollutants in water.[6,7] This heterogeneous photo-Fenton process provides the advantages of low iron ion leaching, low iron sludge

[a] University of Freiburg, Institute and FIT – Freiburg Center for Interactive Materials and Bioinspired Technologies, Georges-Köhler-Allee 105, 79110 Freiburg, Germany. E-mail: severin.vierrath@imtek.uni-freiburg.de
[b] Electrochemical Energy Systems, IMTEK - Department of Microsystems Engineering, University of Freiburg, Georges-Koehler-Allee 103, 79110 Freiburg, Germany
[c] Karlsruhe Nano Micro Facility (KNMFi), Karlsruhe Institute of Technology, Hermann-von-Helmholtz-Platz 1, D-76344 Eggenstein-Leopoldshafen, Germany
[d] Institute for Applied Materials, Energy Storage Systems, Karlsruhe Institute of Technology, Hermann-von-Helmholtz-Platz 1, D-76344 Eggenstein-Leopoldshafen, Germany
[e] Institute of Inorganic and Analytic Chemistry, University of Freiburg, Albertstr. 21, 79104 Freiburg, Germany
[f] Cluster of Excellence livMatS @ FIT – Freiburg Center for Interactive Materials and Bioinspired Technologies, University of Freiburg, Georges-Köhler-Allee 105, D-79110 Freiburg, Germany

† Electronic supplementary information (ESI) available. See DOI: https://doi.org/10.1039/d4ma00196f

formation, a broad pH range of operation, and long-term photocatalyst stability.[8,9]

Despite recent progress, the performance of bare MIL-100(Fe) MOFs in the process of water decontamination is still limited by their available active sites, poor catalytic activity, and low stability.[10,11] To address these issues, various strategies have been employed.[12–18] Loading of metal nanoparticles on MIL-100(Fe) is reported to considerably improve the properties of these MOFs.[13] Nonetheless, one of the challenges of this approach is the aggregation properties of the metal nanoparticles on the surface of MIL-100(Fe), which deactivates the MOFs during continuous photocatalytic cycles. Combining MIL-100(Fe) MOFs with various chemical compounds and the post-treatment of this compound have also been investigated as alternative strategies.[14,15,19] Despite the enhanced performance of MIL-100(Fe) MOFs obtained through these approaches, their preparation requires at least two synthesis steps, which is costly and energy-intensive.

A very promising approach to improve the performance of this compound while overcoming the challenges associated with the previously described strategies is the incorporation of second metal ions into MIL-100(Fe) frameworks to form bimetallic MOFs.[11] Bimetallic MIL-100(Fe,Ni), MIL-100(Fe,Mn), and MIL-100(Fe,Sc) MOFs have been previously synthesized for catalytic reaction purposes.[17,18,20] Despite the potential benefits of these bimetallic MOFs, their industrial production faces two key challenges: first, large-scale synthesis of these bimetallic MOFs would be very costly due to the necessity for high reaction temperatures and special reaction vessels. Second, the synthesis procedures of the mentioned bimetallic MOFs are associated with the utilization of hazardous solvents, such as DMF, HNO_3, and HF, causing potential environmental hazards and additional costs. As a result, there is an undeniable need for a facile, environmentally friendly, and cost-effective method for the production of bimetallic derivatives of MIL-100(Fe) MOFs.

Recently, Steenhaut *et al.*[21] reported a scalable, facile, and green methodology for synthesizing an extensive list of bimetallic MIL-100(Fe,M) MOFs (M consisting of a wide range of p-, d-, and f-elements with M^{1+} to M^{5+} oxidation states) with suitable physicochemical properties. This approach not only facilitates the large-scale and low cost production of the bimetallic MIL-100(Fe,M) MOFs in water and at room temperature, but also allows the incorporation of cationic metals with large ionic radii or oxidation states into MIL-100(Fe) frameworks.

On the basis of this inspiration, herein we substituted the Fe^{3+} cores of MIL-100(Fe) with an element having an initial oxidation state of 2+ (*i.e.* Sn) or 3+ (*i.e.* Ir) to examine the effect of elemental doping on the performance of MIL-100(Fe). Accordingly, a series of bimetallic MIL-100(Fe,Sn) and MIL-100(Fe,Ir) MOFs was synthesized for the first time. The adsorptive and photo-Fenton degradation properties of these bimetallic MOFs were then investigated toward the removal of tetracycline (TC) from aqueous solutions, which is the second most commonly found antibiotic in water.[2,5] Furthermore, a number of characterization techniques were utilized to fully examine the chemical, physical, and electrical characteristics of MIL-100(Fe) and bimetallic MIL-100(Fe,M) MOFs (M: Sn or Ir) in order to elucidate the role of Sn- and Ir-doping on the performance of MIL-100(Fe).

Experimental

Materials

Iron(II) sulfate heptahydrate ($FeSO_4{\cdot}7H_2O$, ≥99%), trimesic acid (H_3BTC, 95%), iridium(III) chloride hydrate ($IrCl_3{\cdot}xH_2O$, 99.9%), tetracycline ($C_{22}H_{24}N_2O_8$, 98%), DMF (C_3H_7NO, 99.8%), nitric acid (HNO_3, 65%), and acetic acid (CH_3COOH, 100%) were purchased from Sigma-Aldrich. Tin(II) chloride dehydrate ($SnCl_2{\cdot}2H_2O$, 98%), and sodium hydroxide (NaOH, 98%) were supplied from Alfa Aesar. Sodium sulfate (Na_2SO_4, ≥99%), hydrogen peroxide (H_2O_2, 30%), and ethanol (C_2H_5OH, 98%) were supplied from Carl Roth GmbH & Co. KG. Nafion D2020 was purchased from FuelCellStore. Indium tin oxide (ITO, 15 Ω sq^{-1})-coated glass was supplied from Colorado Concept Coatings.

Synthesis of the MOFs

MIL-100(Fe) and its bimetallic derivatives were synthesized in two steps according to the procedure reported by Steenhaut *et al.*[21] with some changes, which are described in the sections below.

Synthesis of $Na_3BTC{\cdot}xH_2O$ salt

First, 1.6 g of H_3BTC was added to 20 ml of a 0.3 M NaOH solution and stirred well until complete dissolution of H_3BTC. Next, ethanol was added to the dissolved H_3BTC solution multiple times to eliminate any remaining untreated NaOH, resulting in the formation of $Na_3BTC{\cdot}xH_2O$. Finally, the obtained white fluffy powder was dried overnight in an oven at 80 °C.

Synthesis of MIL-100(Fe) and bimetallic MIL-100(Fe,M) MOFs (M: Sn or Ir)

Synthesis of MIL-100(Fe) was initiated by dissolving 74 mg $Na_3BTC{\cdot}xH_2O$ in 5 ml deionized water, denoted as solution A. Solution B was prepared by adding 90 mg of $FeSO_4{\cdot}7H_2O$ to 5 ml deionized water. These two solutions were mixed overnight under vigorous stirring at room temperature. After 18 h mixing, the resultant precipitate was collected by centrifugation, washed several times with deionized water and ethanol in a water bath set up at 70 °C, and then dried at 80 °C overnight.

The bimetallic MIL-100(Fe,Sn) and MIL-100(Fe,Ir) were synthesized utilizing the same procedure that was applied for the synthesis of MIL-100(Fe) but with the addition of the corresponding dopants to solution B. Different amounts of $SnCl_2{\cdot}2H_2O$ were added to solution B to prepare solutions with Sn^{2+} concentrations of 1.8, 3.5, 7.1, and 14.2 mM, from which MIL-100(Fe,Sn-1.8), MIL-100(Fe,Sn-3.5), MIL-100(Fe,Sn-7.1), and MIL-100(Fe,Sn-14.2) MOFs were synthesized, respectively. Similarly, different amounts of $IrCl_3{\cdot}xH_2O$ were added to the solution B to prepare solutions with Ir^{3+} concentrations of 26.7, 50.2, 62.3, and 100.5 mM, from which MIL-100(Fe,Ir-26.7),

MIL-100(Fe,Ir-50.2), MIL-100(Fe,Ir-62.3), and MIL-100(Fe,Ir-100.5) MOFs were synthesized, respectively.

Characterization

The morphology of the synthesized MOFs was investigated by field emission scanning electron microscopy (FESEM) using an Amber X (Tescan GmbH) system equipped with an Everhart-Thornley detector, operated at 2 kV with a beam current of 100 pA. The samples were mounted on standard aluminium SEM stubs (ScienceServices GmbH) with conductive double-sided adhesive carbon tabs. The particle sizes of the synthesized MOFs were studied by scanning transmission electron microscopy (STEM) using a Talos F200X STEM (ThermoFisher, high-brightness X-FEG emitter) device operated at 200 kV acceleration voltage. For imaging, all samples were prepared by dispersing the MOFs particles in EtOH for 20 min using ultrasonication. Next, several droplets of the dispersed particles were placed onto a copper-based, carbon-coated TEM grid (3–4 nm, 200 mesh, ScienceServices) and air dried prior to mounting on a standard TEM holder (Fischione). Both imaging modes of transmission electron microscopy (TEM) and high-angle annular dark-field scanning transmission electron microscopy (HAADF-STEM) were used for the acquisition of micrographs. In TEM Mode, a beam current of $\sim$1 nA was used; in HAADF-STEM mode, a beam current of $\sim$50 pA and a convergence angle of $\sim$9 mrad were used. The energy dispersive X-ray (EDX) mappings were acquired in STEM-mode with 100 scans and 10 μs dwell time per scan (total acquisition time per sample $\sim$20 min). The X-ray diffraction (XRD) patterns of the MOFs were collected using a Bruker D8 DISCOVER diffractometer equipped with Cu Kα radiation (λ = 1.5418 Å) at a step size of 0.05°. Nitrogen adsorption–desorption measurements were performed on an Autosorb 1-C physisorption station (Quantachrome) operated at 77 K. All samples were degassed at 100 °C for 24 h prior to the measurements. Elemental analysis was conducted on inductively coupled plasma-mass spectrometry (ICP-MS) at Agilent ICP-MS 7500 ce. The samples for the ICP-MS measurements were prepared by complete dissolution of the synthesized MOFs in HNO_3 and CH_3COOH, followed by dilution in deionized water. X-ray photoelectron spectroscopy (XPS) was performed using a K-Alpha+ XPS spectrometer (ThermoFisher Scientific). For data acquisition and processing, Thermo Avantage software was used. All MOFs samples were analyzed using a microfocused, monochromated. Al Kα X-ray source (400 μm spot size). The K-Alpha+ charge compensation system was employed during analysis, using electrons of 8 eV energy and low-energy argon ions to prevent any localized charge build-up. The spectra were fitted with one or more Voigt profiles (BE uncertainty: ±0.2 eV) and Scofield sensitivity factors were applied for quantification.[22] All spectra were referenced to the C 1s peak (C–C and C–H) at 285.0 eV binding energy controlled by means of the well-known photoelectron peaks of metallic Cu, Ag, and Au, respectively. The Fourier-transform infrared (FT-IR) spectra of the MOFs were measured using an Excalibur spectrometer, supplied by Bio-Rad. The ultraviolet-visible (UV-Vis) absorbance spectra of the MOFs particles and TC solution were measured using Agilent Technologies, Cary 60 UV-Vis spectroscopy.

Adsorption and photo-Fenton measurements

The adsorption and photo-Fenton efficiency of MIL-100(Fe) and bimetallic MOFs were investigated toward the removal of TC from aqueous solutions. In a typical experiment, 0.05 g L^{-1} MOFs were added to a 50 mg L^{-1} TC solution and stirred well overnight to reach adsorption–desorption equilibrium. Afterward, 0.05 ml L^{-1} H_2O_2 was added to the mixture, and the mixture was illuminated for 1 h using a solar simulator (100 mW cm^{-2} xenon lamp, Newport) with AM 1.5 G and infrared cut-off filters. The concentrations of TC after dark and light processes were measured using UV-Vis spectroscopy at 355 nm, and the TC removal percentage was calculated according to the following equation:

$$\text{TC removal (\%)} = \frac{C_0 - C_t}{C_0} \times 100 \quad (1)$$

where C_0 (mg L^{-1}) is the initial concentration of TC and C_t (mg L^{-1}) is the concentration of TC after a given time reaction.

Electrochemical measurements

The Mott–Schottky analysis was performed at 1 KHz and in the potential range from −1.0 to +0.2 V *vs.* a calomel electrode (3.5 M KCl). The measurements were carried out in a 0.2 M Na_2SO_4 solution using a CH instrument electrochemical workstation connected to the calomel reference electrode, a platinum mesh counter electrode (2.5 × 2.5 cm^2), and a working electrode. For the preparation of the working electrode, an ITO substrate was first cleaned by sonication in a water/acetone (*v*/*v* = 50/50) mixture for 10 min and then dried at 80 °C. The surface of the ITO substrate was then covered with Scotch tape except for the 30 mm^2 active area left for the deposition of the MOFs slurry. The MOFs slurry was prepared by dispersing 3 mg of MOFs in a mixture of 300 μl DMF and 15 μl Nafion overnight. Then, the prepared ITO substrate was placed on a hotplate at 80 °C, and 15 μl of the slurry was drop-casted onto the bare area of the substrate. Once the deposited slurry on the ITO substrate was dried, the Scotch tape was removed, and an electrical connection was made to the modified substrate using copper conductive tape. Finally, the inactive area of the modified substrate was sealed and isolated with epoxy resin.

Results and discussion

Possible chemical structures of the bimetallic MIL-100(Fe,M) MOFs (M: Sn or Ir)

Scheme 1 illustrates the possible chemical structures of the synthesized MOFs. As investigated previously,[21] metals with oxidation states II or III is accommodated into the framework of MIL-100(Fe) by varying the nature of the oxygenated ligand on the doping metal site. Therefore, if we assume that only one doping metal ion is present in the M_3-μ_3-oxo cluster of the bimetallic MOFs at the maximum, the tin atom of the MIL-100(Fe,Sn) does not require any counter ion (Scheme 1, bottom-left),

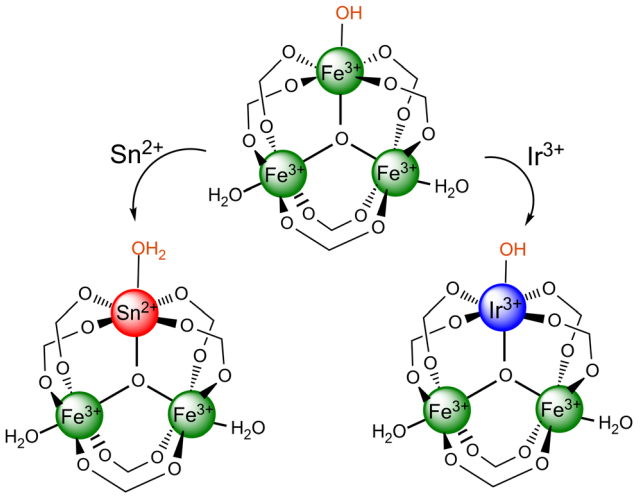

Scheme 1 MII-100(Fe) (up-middle), MIL-100(Fe,Sn) (bottom-left), and MIL-100(Fe,Ir) (bottom-right).

while the iridium atom of the MIL-100(Fe,Ir) is balanced by an OH^- group (Scheme 1, bottom-right).[21]

Adsorptive and photo-Fenton removal efficiency of the bimetallic MIL-100(Fe,M) MOFs (M: Sn or Ir)

As described in the experimental section, a series of bimetallic MIL-100(Fe,Sn) MOFs and MIL-100(Fe,Ir) MOFs with different concentrations of each dopant was synthesized, and their performances were examined toward the removal of TC from an aqueous solution. Fig. 1a and Table S1 (ESI†) show the TC removal (%) of MIL-100(Fe), MIL-100(Fe,Sn) series, and MIL-100(Fe,Ir) series in the dark (Fig. 1a, grid columns in grey) and under photo-Fenton (Fig. 1a, solid columns in orange) conditions. In the absence of light, the synthesized MOFs reached the adsorption–desorption equilibrium after 18 hours, indicating their slow adsorption kinetics. The maximum dark adsorption of about 13% was obtained for MIL-100(Fe) which was close to that of the bimetallic MIL-100(Fe,Sn) MOFs series. In contrast, the TC removal efficiencies of the bimetallic MIL-100(Fe,Ir) series in the dark were significantly higher than that of MIL-100(Fe) and bimetallic MIL-100(Fe,Sn) MOFs series, reaching a maximum of about 52% in the case of MIL-100(Fe,Ir-100.5).

After adsorption under dark conditions, the photo-Fenton degradation efficiencies of the synthesized MOFs were evaluated. In this step, the photo-Fenton process was initiated by the addition of H_2O_2 to the reaction medium, followed by illumination. Upon illumination, highly active hydroxyl radicals are generated that attack TC molecules.[23] It is important to note that the concentrations of H_2O_2 is an important parameter that affects the efficiency of the degradation process. Previous studies have demonstrated,[11,24,25] the amount of free hydroxyl radicals and, thus, the catalytic efficiency rises upon the increase in H_2O_2 concentration within a certain concentration range. However, at high H_2O_2 concentrations, hydroxyl radicals are trapped by H_2O_2, resulting in the formation of perhydroxyl

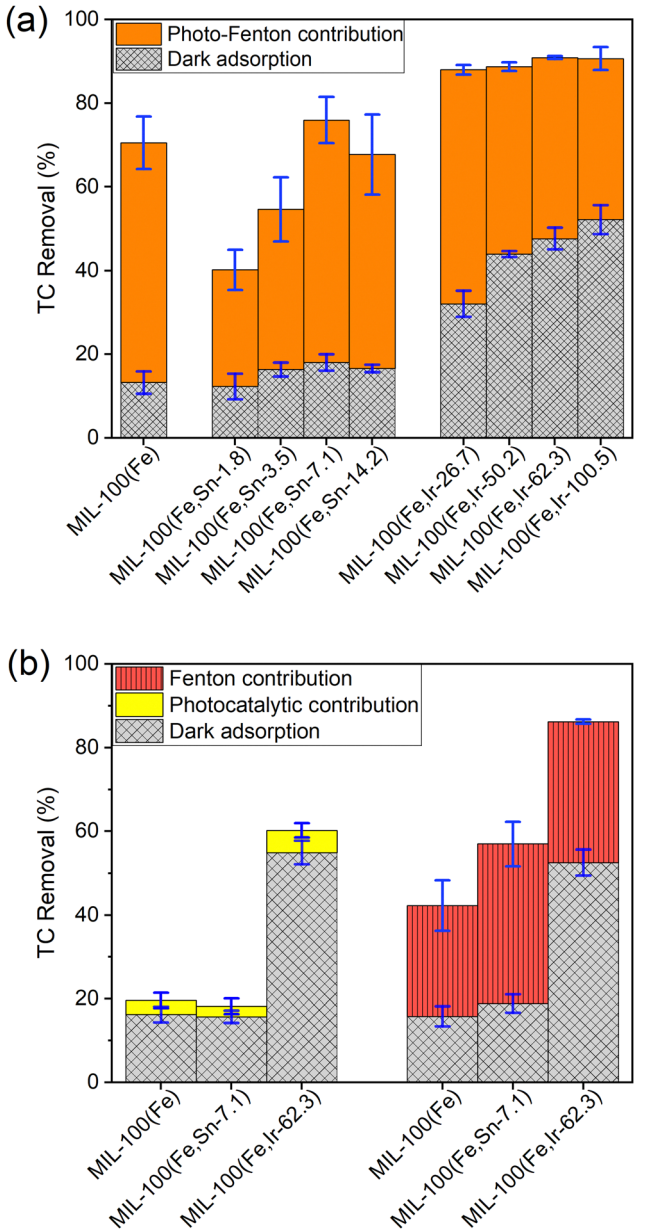

Fig. 1 (a) TC removal (%) of MIL-100(Fe), MIL-100(Fe,Sn) series, and MIL-100(Fe,Ir) series under dark (grid columns in grey) and under photo-Fenton (solid columns in orange) conditions. (b) Comparison of the TC removal *via* adsorption (grid columns in grey), photocatalytic (solid columns in yellow), and Fenton processes (vertically hatched columns in red) for MIL-100(Fe), MIL-100(Fe,Sn-7.1), and MIL-100(Fe,Ir-62.3). The experiments were carried out using 50 mg L^{-1} TC and 0.05 g L^{-1} of each MOFs. For the photo-Fenton and Fenton experiments, 0.05 ml L^{-1} H_2O_2 was added to the reaction vessel.

radicals with weaker oxidative effect. Consequently, for consistency and comparability, a constant concentration of H_2O_2 was maintained throughout this study.

The obtained results showed that the photo-Fenton degradation efficiency of the bimetallic MIL-100(Fe,Sn) MOFs increased from 28% to 58% with the increase in Sn^{2+} concentration from MIL-100(Fe,Sn-1.8) to MIL-100(Fe,Sn-7.1) (Fig. 1a). A further increase of the Sn^{2+} concentration, however, resulted

in a decrease in the TC degradation efficiency to 51% in the case of MIL-100(Fe,Sn-14.2). The observed differences in the photo-Fenton efficiency may be ascribed to possible changes in specific surface area, band gap energy, and lifetime of the photogenerated carriers upon variations in the Sn^{2+} content of the bimetallic MIL-100(Fe,Sn) MOFs.[11,18,26,27]

In contrast, the photo-Fenton activities of the bimetallic MIL-100(Fe,Ir) MOFs series gradually reduced upon increasing their Ir^{3+} content. This could be due to the steadily increase in the adsorption property of the bimetallic MIL-100(Fe,Ir) MOFs as the Ir^{3+} content raised, which resulted in more and more accumulation of TC at the photocatalyst surface and blockage of light from reaching the active sites of the photocatalyst, hence the gradual decrease in the photo-Fenton activity.[28,29]

Among the bimetallic MOFs, MIL-100(Fe,Sn-7.1) and MIL-100(Fe,Ir-62.3) showed the highest overall performance in their respective series, with TC removal efficiencies of 76% and 91%, respectively. Under the same experimental conditions, the TC removal efficiency of MIL-100(Fe) was 71%. It can thus be concluded that the Sn-doping only slightly improves the performance of MIL-100(Fe) toward the TC degradation, while Ir-doping substantially increases the removal performance by enhancing the adsorption property of MIL-100(Fe). In comparison to the previously reported results,[11] in this work, 0.05 g L^{-1} MIL-100 (Fe,Ir-62.3) and 0.05 ml L^{-1} H_2O_2 were used to achieve the TC removal efficiency of 91% in a solution containing 50 mg L^{-1} TC, whereas in the work reported by Guo *et al.*,[11] similar removal efficiency was obtained in the presence of 0.2 g L^{-1} MIL-100 (Fe) and 20 ml L^{-1} H_2O_2.

To evaluate the exclusive contribution of light or H_2O_2 on the performance of the synthesized MOFs, the photocatalytic activities of the best-performing MOFs from each bimetallic series, *i.e.* MIL-100(Fe,Sn-7.1) and MIL-100(Fe,Ir-62.3), were examined: (a) in the presence of light and absence of H_2O_2 (photocatalytic contribution) and (b) in the presence of H_2O_2 (Fenton contribution) under dark conditions. As can be seen from Fig. 1b, the contribution of the Fenton degradation (vertically hatched columns in red) is substantially higher than the photocatalytic degradation process (solid columns in yellow), indicating that the synthesized MOFs are more active in the Fenton-like process.[30] It is worth noting that the light and Fenton degradation of TC in the absence of MOFs particles were negligible (less than 1%).

In order to understand the effects of Sn and Ir-doping on the adsorptive and photo-Fenton properties of MIL-100(Fe), the best-performing MOFs from each bimetallic series, MIL-100(Fe,Sn-7.1) and MIL-100(Fe,Ir-62.3), were chosen for further investigation in this work, and their physicochemical properties were compared to those of MIL-100(Fe).

Structural properties of the bimetallic MIL-100(Fe,M) MOFs (M: Sn or Ir)

SEM, TEM, and elemental analysis. The shape, size, and elemental composition of MIL-100(Fe) and its bimetallic variants were investigated using electron microscopy. As can be seen from Fig. 2a and b, the synthesized MIL-100(Fe) and MIL-100(Fe,Sn-7.1) consist of octahedral particles within the range of 400–800 nm, which is in good agreement with previous studies.[11,31] In comparison to these particles, the MIL-100(Fe,Ir-62.3) particles were about ten times smaller (Fig. 2c). These observations were also confirmed by the TEM images of these MOFs (Fig. 2d–f).

Fig. 3 shows the HAADF-STEM images and the elemental mapping analysis of the synthesized MOFs. The individual elemental mapping indicated that Fe, C, and O were all uniformly present in MIL-100(Fe), MIL-100(Fe,Sn-7.1), and MIL-100(Fe,Ir-62.3). For the case of MIL-100(Fe,Sn-7.1), some Sn inhomogeneity was observed on the surface of the particles

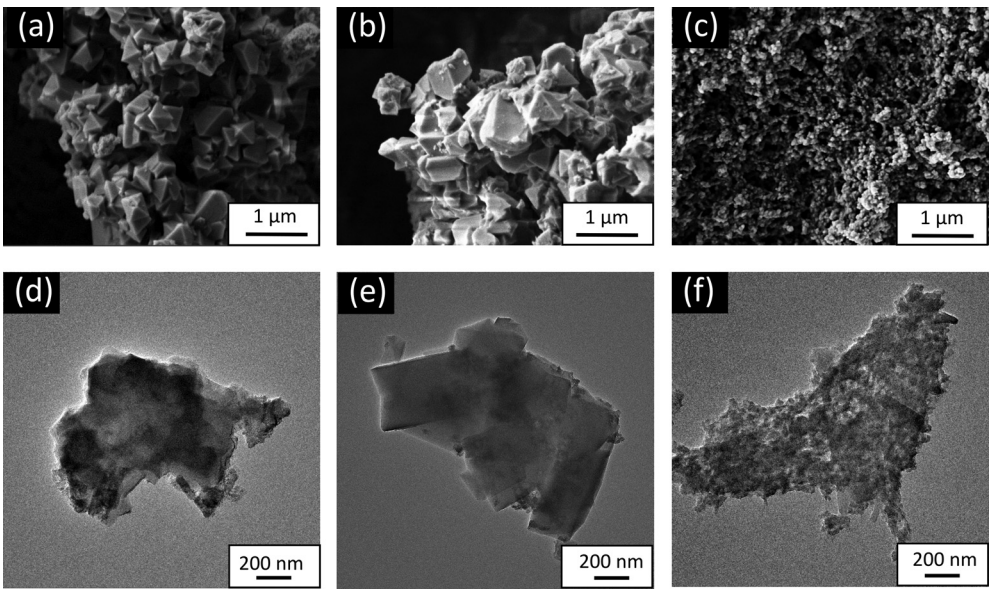

Fig. 2 SEM (upper row) and TEM (bottom row) image of the (a) and (d) MIL-100(Fe), (b) and (e) MIL-100 (Fe,Sn-7.1), and (c and f) MIL-100(Fe,Ir-62.3).

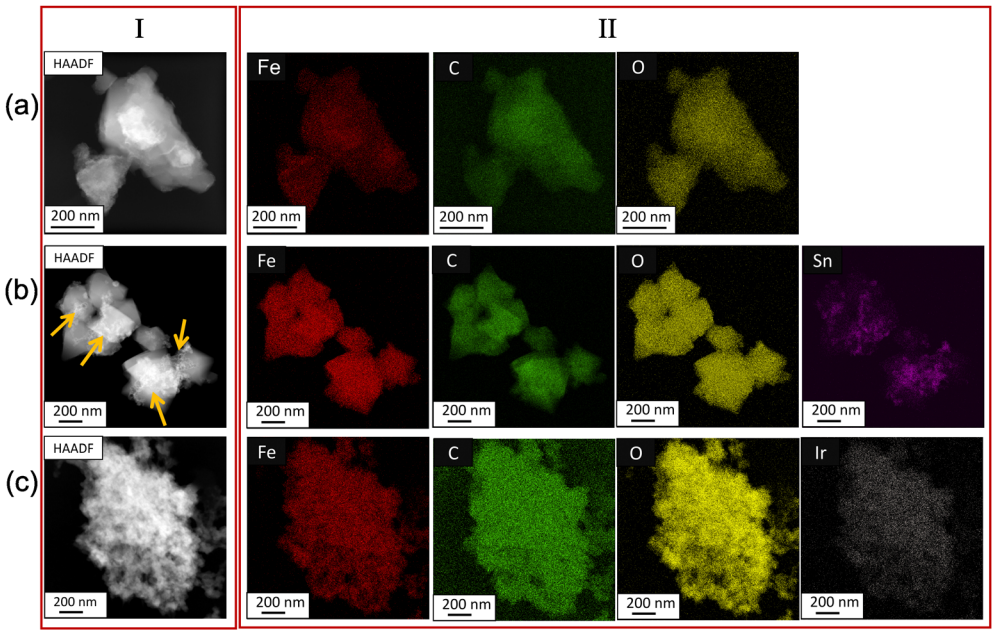

Fig. 3 (I) HAADF-STEM images and (II) EDX elemental mapping of the (a) MIL-100(Fe), (b) MIL-100(Fe,Sn-7.1), and (c) MIL-100(Fe,Ir-62.3).

(Fig. 3b, indicated by orange arrows). In contrast, the Ir distribution of MIL-100(Fe,Ir-62.3) was homogeneous (Fig. 3c). This variation in dopant distribution of the bimetallic MOFs particles was previously studied by Steenhaut *et al.*[21] They reported that elements with oxidation state of 2+, *i.e.* Sn^{2+} in our case, are more on the surface than in the core of bimetallic MOFs crystals. In contrast, elements with an oxidation state of 3+, *i.e.* Ir^{3+} in our case, are incorporated preferentially over Fe^{3+} in the bimetallic MIL-100(Fe,M), resulting in a higher bulk than the surface concentration of Ir.

Using ICP-MS measurement, the exact amounts of doping metals in the bulk of bimetallic MOFs were assessed, and the results are presented in Table S2 (ESI†). When a solution with a Sn mol ratio ($mol_{Sn}/(mol_{Sn} + mol_{Fe})$) of 9.9% was used, MIL-100(Fe,Sn-7.1) with a Sn mol ratio of 3.6% was obtained. When an Ir mol ratio ($mol_{Ir}/(mol_{Ir} + mol_{Fe})$) of 49% was used, the Ir mol ratio of about 1.5 mol% was obtained for the synthesized MIL-100(Fe,Ir-62.3). This indicates the higher incorporation of Sn^{2+} into MIL-100(Fe) framework than of Ir^{3+} under the applied conditions.

XRD analysis. The XRD patterns of MIL-100(Fe) and bimetallic MIL-100(Fe,M) MOFs are shown in Fig. 4. Consistent with the previously reported results, the characteristic peaks of MIL-100(Fe) were observed at 2θ = 3.4°, 4.0°, 6.2°, 10.7°, 11.3°, 12.5°, 14.6°, 20.5°, 24.5°, and 28.3°.[10,32] The XRD patterns of MIL-100(Fe,Sn-7.1) and MIL-100(Fe,Ir-62.3) were matched well with those of MIL-100(Fe), implying that the synthesis of the bimetallic MOFs were successful and that no iron oxide impurities were produced during their synthesis process (full XRD patterns can be found in Fig. S1, ESI†).[21] In the case of MIL-100(Fe) and MIL-100(Fe,Sn-7.1), sharp diffraction peaks were observed in their XRD patterns, indicating the high degree of crystallinity of these samples. In contrast, less intense and

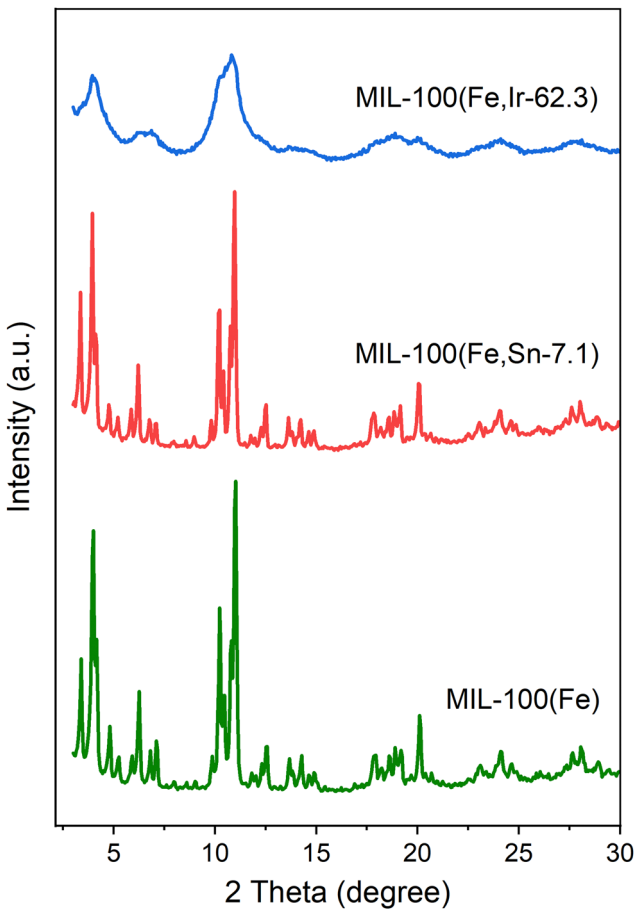

Fig. 4 XRD spectra of the MIL-100(Fe), MIL-100(Fe,Sn-7.1), and MIL-100(Fe,Ir-62.3).

broader signals were detected in the XRD pattern of MIL-100(Fe,Ir-62.3). This can be related to the smaller crystallite sizes of MIL-100(Fe,Ir-62.3) compared to those of the MIL-100(Fe) and MIL-100(Fe,Sn-7.1), in line with the smaller particle sizes observed by SEM and TEM.

FT-IR, UV-Vis, and band gap analysis. FT-IR spectroscopy was employed to explore probable alterations in the functional groups of MIL-100(Fe) after being doped with Sn^{2+} or Ir^{3+}. Additionally, the potential chemical interaction between the TC molecules and the synthesized MOFs during the dark adsorption process was investigated using these techniques. As can be seen from Fig. 5a, MIL-100(Fe), MIL-100(Fe,Sn-7.1), and MIL-100(Fe,Ir-62.3) MOFs exhibited similar peaks comparable to those previously reported for MIL-100(Fe) MOFs.[21,33] The characteristic peaks of the Fe–O and Fe–O–Fe vibrations were detected at about 460 and 610 cm^{-1}, respectively, indicating the formation of iron–oxo clusters between the tricarboxylate linkers and Fe^{3+} nodes. The stretching vibrations of the C=C and C=O bonds of the tricarboxylate linkers were observed at 1370, 1450, and 1616 cm^{-1}. Also, the band at about 1703 cm^{-1} corresponding to the presence of unreacted tricarboxylate linkers was detected in the spectra of the samples.[34] The characteristic band ranging from 1900 to 2250 cm^{-1} are related to the atmospheric CO_2 molecules. The broad band that appeared at about 3300 cm^{-1} is attributed to the O–H stretching vibration of water molecules.

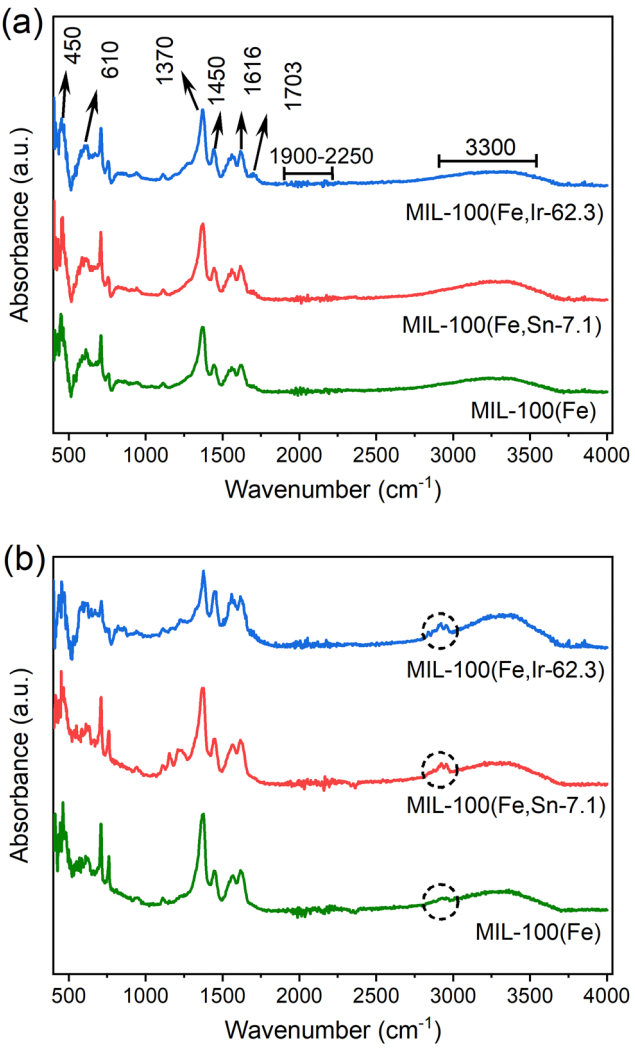

Fig. 5 FT-IR spectra of MIL-100(Fe), MIL-100(Fe,Sn-7.1), and MIL-100(Fe,Ir-62.3) (a) before and (b) after the adoption of TC.

After TC adsorption, the N–H vibration bands (indicated with circles in Fig. 5b) appeared in the FT-IR spectra of the synthesized MOFs in the region between 2800 cm^{-1} and 3000 cm^{-1}.[35] Its important to note that the TC may be entrapped in the MOFs pores or adsorbed on MOFs through hydrogen bonding between the $-NH_2$ groups of TC and the -OH groups of the MOFs.[33]

The optical properties of MIL-100(Fe) and bimetallic MOFs were assessed using UV-Vis spectroscopy. As shown in Fig. 6, the absorption spectra of the synthesized MOFs revealed two absorption bands: a band at about 240 nm and a second absorption band with a maximum at about 320 or 350 nm, which is extended to the visible region.[34,36] These bands correspond to the ligand-to-metal charge transfer within the MOFs.

The optical band gaps of MIL-100(Fe) and the bimetallic MOFs were calculated using Tauc equation as follows:[37]

$$(\alpha h\nu)^2 \sim (h\nu - E_g) \quad (2)$$

where α, h (eV s), ν (s^{-1}), are the absorption coefficient, Planck constant, and the light frequency, respectively. E_g is the band gap of the photocatalyst.

As shown in the inset of Fig. 6a, the band gap of about 2.7 eV was estimated for MIL-100(Fe), which is in good agreement with previous reports.[10,11] Incorporation of Sn, however, reduced the band gap of MIL-100(Fe) to 2.3 eV (inset of Fig. 6b). The band gap of MIL-100(Fe), on the other hand, increased to about 3.3 eV by Ir doping (inset of Fig. 6c), which would enhance the utilization of UV light during the photocatalytic processes.

Nitrogen adsorption–desorption analysis. The nitrogen adsorption–desorption isotherms and pore size distribution curves of the synthesized MOFs are shown in Fig. 7. According to the IUPAC classification, MIL-100(Fe) and MIL-100(Fe,Sn-7.1) MOFs exhibited an isotherm of type IV with a distinct H4 hysteresis loop (Fig. 7a and b).[38] The rapid intake of nitrogen with two uptakes near P/P^0 = 0.05 and 0.13 obtained for MIL-100(Fe) and MIL-100(Fe,Sn-7.1) demonstrates the presence of microporous windows (about 2 nm) and mesoporous cages (about 3 nm) (Fig. 7a and b, insets). The adsorption–desorption curve of MIL-100(Fe,Ir-62.3) (Fig. 7c) showed a mixture of type I and IV isotherms with two moderate uptakes at low relative pressures (Fig. S2, ESI†), identical to that of the MIL-100(Fe) and MIL-100(Fe,Sn-7.1), indicating the presence of micropores in MIL-100(Fe,Ir-62.3). In addition, a sharp increase in nitrogen adsorption with a narrow hysteresis loop at relatively high pressures was observed for MIL-100(Fe,Ir-62.3), which could be related to mesoporous interparticle porosity (Fig. 7c, inset).

The Brunauer, Emmett, and Teller (BET) method was then utilized to estimate the specific surface area of the MOFs.

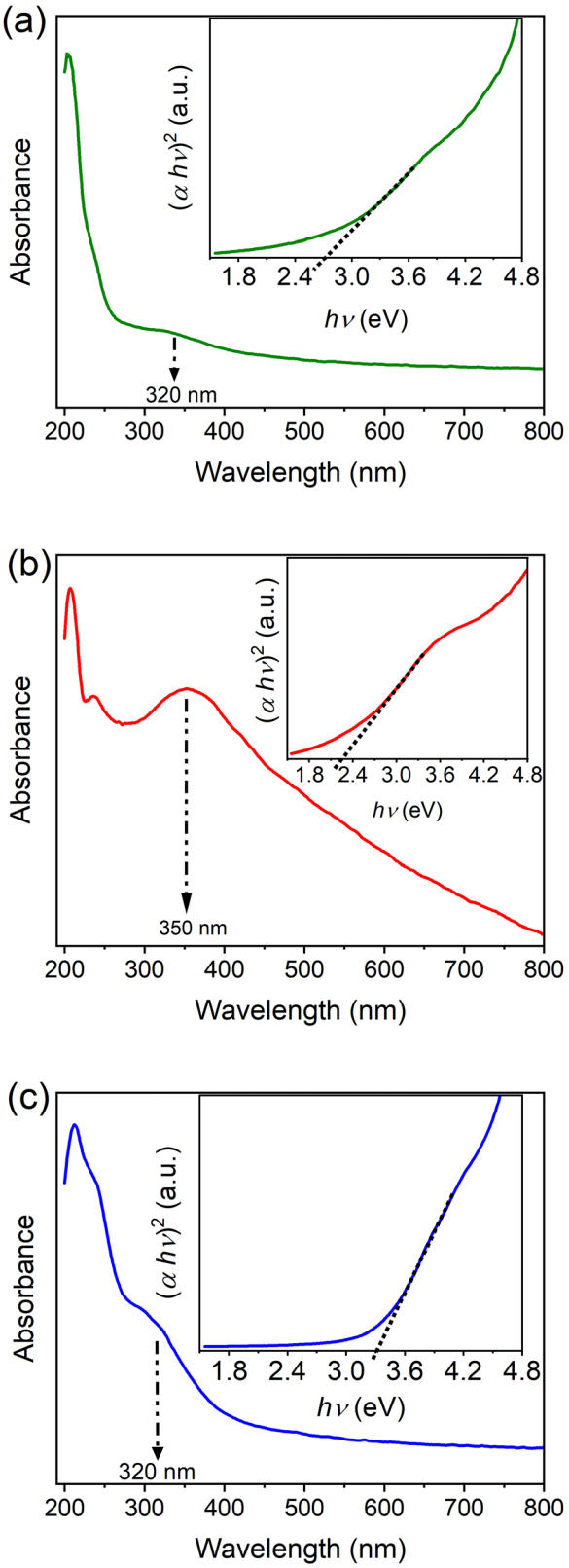

Fig. 6 UV-Vis spectra and optical band gap energy of (a) MIL-100(Fe), (b) MIL-100(Fe,Sn-7.1), and (c) MIL-100(Fe,Ir-62.3).

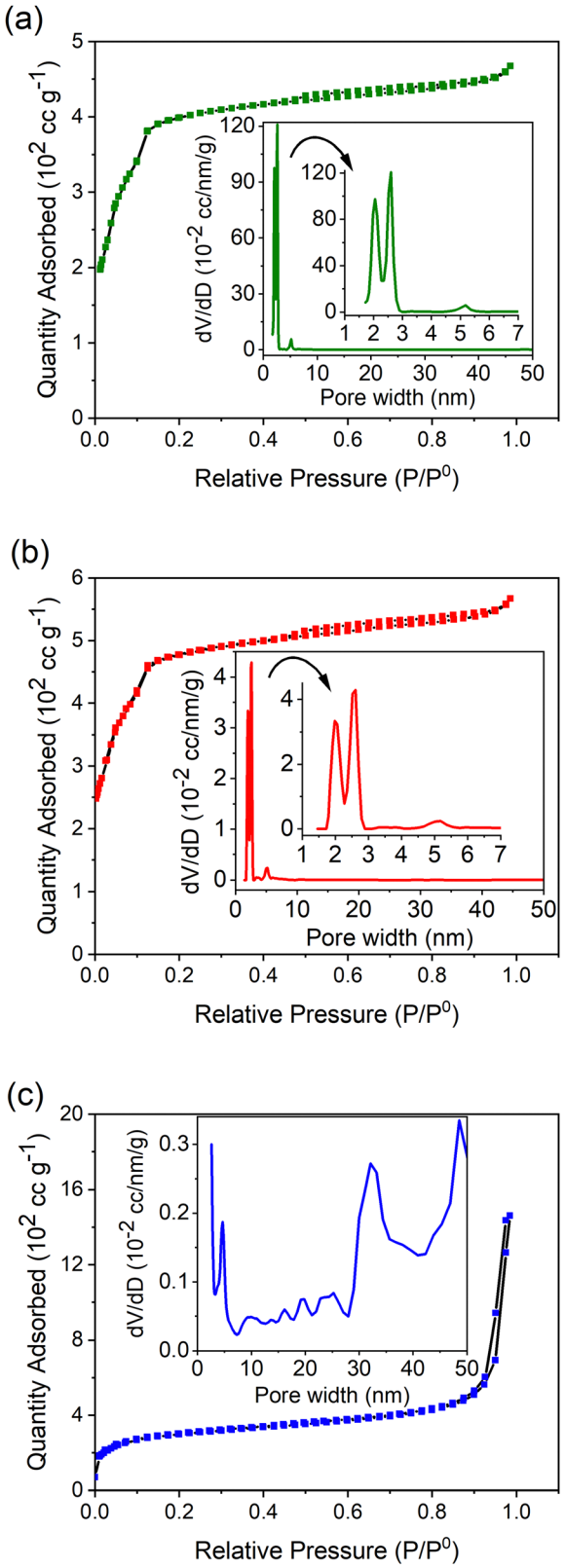

Fig. 7 Nitrogen adsorption–desorption isotherms of the (a) MIL-100(Fe), (b) MIL-100(Fe,Sn-7.1), and (c) MIL-100(Fe,Ir-62.3). The insets show the corresponding pore-size distribution curve calculated from the adsorption branch of the nitrogen isotherm.

Table 1 BET surface area, average pore diameter, and total pore volume of the MOFs

MOFs	BET surface area ($m^2\ g^{-1}$)	Average pore diameter (nm)	Total pore volume (cc g^{-1})
MIL-100(Fe)	1536	1.88	0.72
MIL-100(Fe,Sn-7.1)	1779	1.98	0.88
MIL-100(Fe,Ir-62.3)	1096	8.24	2.26

Table 1 summarizes the calculated values of the BET surface area, average pore diameter, and total pore volume of the synthesized MOFs. The BET surface area of MIL-100(Fe) was calculated to be 1536 $m^2\ g^{-1}$. MIL-100(Fe,Sn-7.1) exhibited the largest BET surface area (1779 $m^2\ g^{-1}$), whereas MIL-100(Fe,Ir-62.3) showed the lowest BET surface area (1096 $m^2\ g^{-1}$) among the measured MOFs. According to Steenhaut *et al.*,[21] doping MIL-100(Fe) with metal ions having an oxidation state of 2+ (*i.e.* Sn^{2+} in this work) more likely enhances the surface area of MIL-100(Fe) than doping with metal ions with an oxidation state of 3+ (*i.e.* Ir^{3+} in this work).

The fact that MIL-100(Fe,Ir-62.3) with the lowest surface area showed the highest adsorption property toward TC molecules (Fig. 1) indicates that a parameter different than the BET surface area should be responsible for the enhanced adsorption property of MIL-100(Fe,Ir-62.3). The large average pore diameter and total pore volume of MIL-100(Fe,Ir-62.3) compared to the other MOFs (Table 1) are assumed to be the key factors determining the superior adsorption property of MIL-100(Fe,Ir-62.3).[39] MIL-100(Fe) and MIL-100(Fe,Sn-7.1) with comparable average pore diameter and total pore volume showed also comparable adsorption efficiency.

XPS analysis. The chemical composition and oxidation state of the elements at the surface of the synthesized MOFs were determined using XPS analysis. The full-range XPS survey spectra in Fig. 8a confirmed that MIL-100(Fe) and its bimetallic derivatives are mainly composed of C and O elements. The C 1s spectra were deconvoluted into two peaks, one at 285.0 eV and a second one at 289.1 eV, corresponding to the C–H, C=C, and –COOH moieties of the BTC ligand (Fig. 8b) respectively.[40] The broad O 1s spectra consisted of three peaks at 530.5, 532.2, and 534.0 eV detected for all samples (Fig. 8c), which are attributed to the Fe–O clusters and oxygen groups of the BTC ligands. Deconvolution of the Fe $2p_{3/2}$ spectra (Fig. 8d) using the multiplet approach described by Biesinger *et al.*[41] indicated the presence of Fe in two oxidation states, namely Fe^{2+} (peaks in grey) and Fe^{3+} (peaks in black), in these samples. This observation revealed that around 40% of the total iron detected at the surface of the synthesized MOFs exist as Fe^{2+}, which may be the unreacted Fe^{2+} species of the precursor or the ferrous hydroxide formed during the synthesis. In the case of MIL-100(Fe,Sn-7.1), the Sn $3d_{5/2}$ peak was detected as expected at about 487.2 eV (Fig. 8e). However, this peak individually cannot be used to determine the oxidation state of Sn, and further analysis utilizing the valence band spectrum or Auger peak is required. Since less than 1% of the Sn was detected in this sample, the exact determination of Sn oxidation state was not possible.[42]

In the case of MIL-100(Fe,Ir-62.3), the Ir $4f_{7/2}$ and Ir $4f_{5/2}$ peaks of the expected doublet were clearly observed at about 63.2 and 66.2 eV, respectively (Fig. 8f). In comparison to the XPS spectra of the reference $IrCl_3 \cdot xH_2O$ sample, we observed a slight shift of about 0.5 eV (indicated by an arrow) toward higher binding energy for MIL-100(Fe,Ir-62.3) sample, suggesting the presence of Ir^{4+} in addition to Ir^{3+} in this sample.[43]

Plausible TC removal mechanism

The elimination of TC from aqueous solutions using the synthesized MOFs is divided into two phases: (I) diffusion of TC molecules from the bulk of the solution to the surface and interior of the MOFs particles followed by their adsorption on their atomically constructed surface; and (II) photo-Fenton degradation of the adsorbed TC at the surface of the MOFs. While the former factor is mostly related to the characteristics of the MOFs pores, the latter factor is influenced by the light absorption ability of the MOFs, the lifetime of photo-generated charges, and the quantity of the generated hydroxyl radical ($OH^{\bullet}$) species.

The adsorption process is initiated by the dispersion of MOFs molecules into the TC solution, which proceeds overnight until the adsorption–desorption equilibrium is reached. In this step, the accessibility of MOFs sites and the dimension of their pores in comparison to the TC molecular size[44] are critical. According to the FTIR measurements, the TC adsorption properties of the best-performing MOFs of this work *via* chemical interaction were similar. However, the highest adsorption performance was obtained for MIL-100(Fe,Ir-62.3), most likely due to its larger average pore size and pore volume than that of MIL-100(Fe) and MIL-100(Fe,Sn-7.1).

In the second step, the photo-Fenton degradation of TC is started by the addition of H_2O_2 to the reaction vessel under illumination. As a result of light absorption by the tricarboxylate ligands and electron transfer from ligands to Fe^{3+} nodes, electrons and holes are generated within the MOFs (3). The photogenerated electrons can reduce MIL-100(Fe^{3+}) to MIL-100(Fe^{2+}) (4). The electrons with an appropriate life-time may also be captured by oxygen molecules, producing superoxide radicals (5). Regeneration of MIL-100(Fe^{3+}) by H_2O_2 results in the formation of highly active hydroxyl radicals *via* the Fenton-like reaction (6). Another possible route for the generation of hydroxyl radicals can be *via* the interaction of water molecules with photogenerated holes (7), though it is widely accepted that the hydroxyl radicals are mainly generated *via* the Fenton reaction.[12,45] Finally, TC is degraded into smaller molecules by reactive oxidation species (8). Within the array of oxidative species discussed earlier, hydroxyl radicals were determined as pivotal agents in the photo-Fenton degradation mechanism of TC.[11,46] The possible photo-Fenton pathways toward the degradation of TC in the presence of MIL-100(Fe) and the majority of the products formed during this process have been previously investigated by Li *et al.*[46] They reported that, the most intermediates produced during this process have lower developmental toxicity and higher bioaccumulation factor than the initial TC.[46]

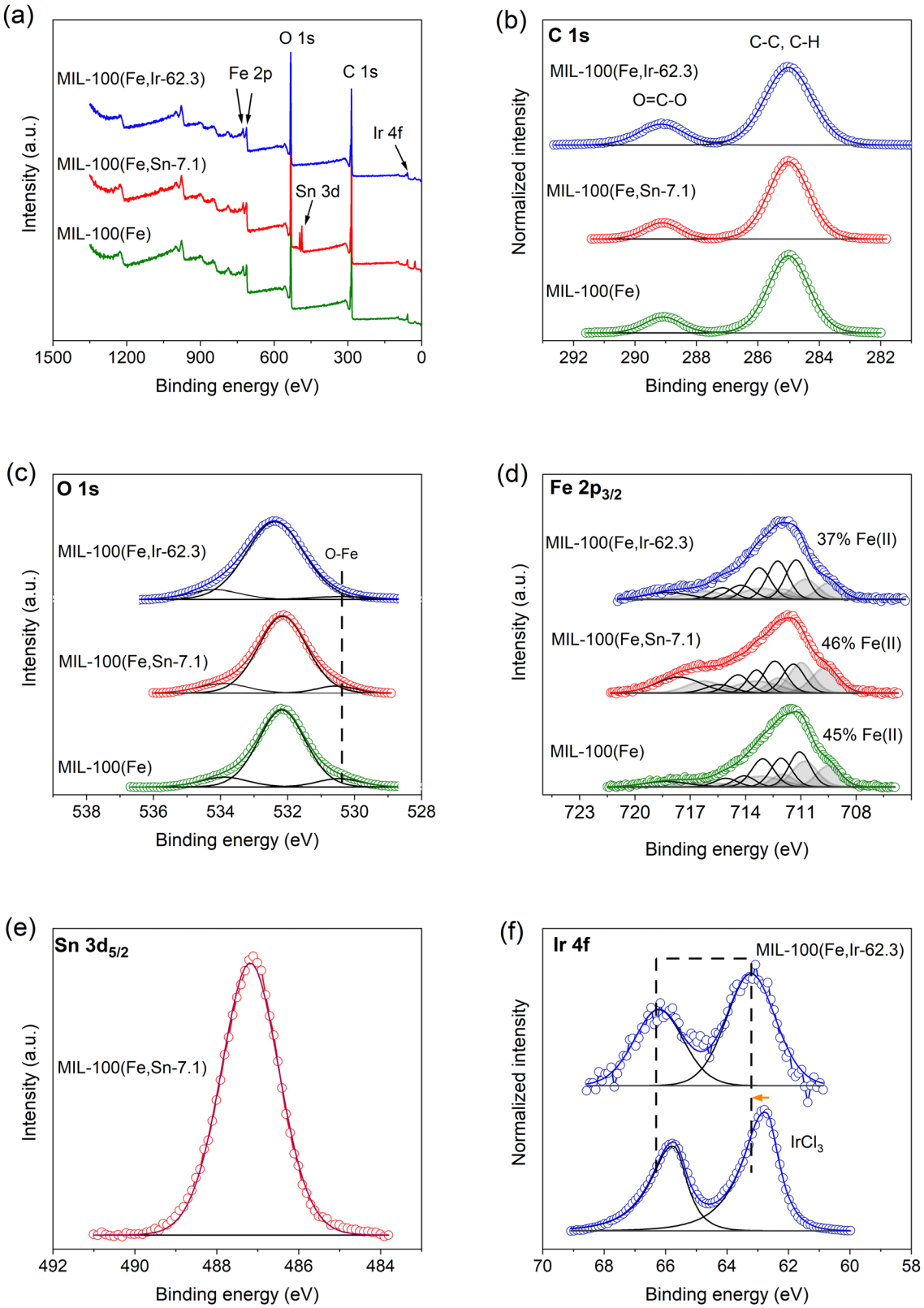

Fig. 8 XPS (a) survey spectra, (b) C 1s, (c) O 1s and (d) Fe $2p_{3/2}$ spectra of MIL-100(Fe), MIL-100(Fe,Sn-7.1), and MIL-100(Fe,Ir-62.3). (e) Sn $3d_{5/2}$ spectrum of MIL-100(Fe,Sn-7.1). (f) Ir 4f spectrum of MIL-100(Fe,Ir-62.3) compared to the reference $IrCl_3 \cdot xH_2O$.

$$\mathrm{MIL-100(Fe^{3+})} + h\nu \rightarrow \mathrm{MIL-100(Fe^{3+})} + e^- + h^+ \quad (3)$$

$$\mathrm{MIL-100(Fe^{3+})} + e^- \rightarrow \mathrm{MIL-100(Fe^{2+})} \quad (4)$$

$$e^- + O_{2(ads.)} \rightarrow O_2^{\bullet -} \quad (5)$$

$$\mathrm{MIL-100(Fe^{2+})} + H_2O_2 \rightarrow \mathrm{MIL-100(Fe^{3+})} + OH^- + OH^{\bullet} \quad (6)$$

$$h^+ + H_2O \rightarrow H^+ + OH^{\bullet} \quad (7)$$

$$h^+/O_2^{\bullet -}/OH^{\bullet} + \mathrm{TC} \rightarrow \text{degradation products} \quad (8)$$

To have a better understanding of the photocatalytic activity of the best-performing MOFs toward the removal of TC, Mott–Schottky analysis was carried out.[47] As illustrated in Fig. 9a, the flat band potentials of the best-performing MOFs were estimated using the Mott–Schottky curve. The positive slope of the Mott–Schottky curves indicated that all the MOFs are n-type semiconductors, for which their flat band potentials are very close to their conduction bands.[14] Using the band gap energies determined from the Tauc plots, the conduction band of MIL-100(Fe), MIL-100(Fe,Sn-7.1), and MIL-100(Fe,Ir-62.3) MOFs was estimated as −0.50, −0.50, and −0.55 eV *vs.* RHE, respectively (Fig. 9b). As the conduction bands of the MOFs are more negative than the standard reduction potential of oxygen (−0.35 ± 0.02 eV *vs.* NHE at pH 7),[48,49] transfer of photogenerated electrons to the adsorbed oxygen molecules and the formation of superoxide radicals are thermodynamically permissible on all MOFs samples. Although MIL-100(Fe,Ir-62.3) has a large band gap energy of around 3.3 eV, the most negative conduction band potential of this photocatalyst among the synthesized MOFs seems to be responsible for its high photocatalytic activity toward elimination of TC compared to the other MOFs studied in this work (Fig. 1b, solid columns in yellow).

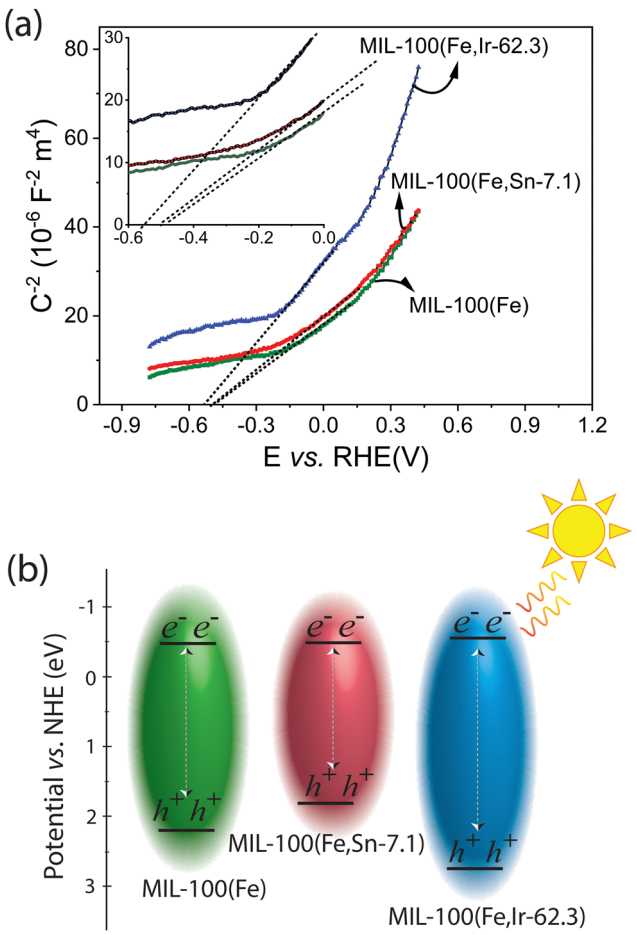

Fig. 9 (a) Representative Mott–Schottky plots for MIL-100(Fe), MIL-100(Fe,Sn-7.1), and MIL-100(Fe,Ir-62.3) MOFs. The Mott–Schottky analysis was performed at 1 KHz and in the potential range from −1.0 to +0.2 V *vs.* a calomel electrode (3.5 M KCl) in 0.2 M Na_2SO_4 solution. The inset shows the plots in the potential range from −0.6 V to 0.0 V. (b) Schematic band diagram of the synthesized MOFs.

Reusability of the bimetallic MIL-100(Fe,M) MOFs (M: Sn or Ir)

In addition to the contaminant removal and degradation efficiency of MOFs, their stability and reusability are also important. Indeed, producing and destroying massive quantities of MOFs for large-scale applications poses a variety of economic and environmental challenges. Therefore, it is important to synthesize MOFs-based compounds that are recyclable and reusable multiple times.

In this work, the reusability of the synthesized MOFs were studied for three cycles under the same experimental conditions that are described in the experimental section without applying any regeneration procedure. As shown in Fig. 10, it can be distinctly observed that the removal efficiency of the synthesized MOFs gradually decreased after each cycle. It is expected that when the MOFs are not regenerated after each photocatalytic cycle, the accumulated TC molecules and degradation products inside the pore or on the surface of the photocatalysts significantly reduce the removal efficiency in the next cycle. Among the studied MOFs, the rate of performance deterioration was more pronounced for MIL-100(Fe,Ir-62.3), which might be attributed to the higher saturation or blockage of its pores with TC molecules after each cycle.

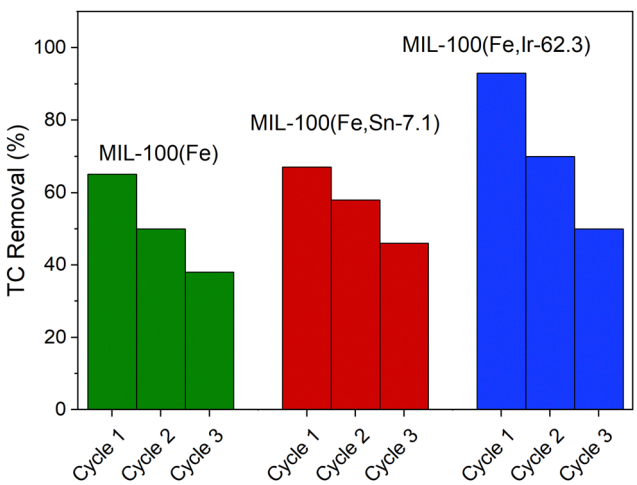

Fig. 10 Reusability of MIL-100(Fe), MIL-100(Fe,Sn-7.1), and MIL-100(Fe,Ir-62.3) for three consecutive cycles.

In comparison to the previously reported MIL-100(Fe)-based photocatalysts,[11,50] the reusability efficiencies of the studied MOFs in this work are notable, as TC removal efficiencies of approximately 40% were observed even after three cycles and without employing any regeneration procedure between cycles (Fig. 10).

Conclusions

In this work, MIL-100(Fe) and a series of bimetallic MIL-100(Fe,Sn) MOFs and bimetallic MIL-100(Fe,Ir) MOFs were synthesized *via* a green synthesis method in DI water and at room temperature. The dark and photo-Fenton activities of the synthesized MOFs were assessed toward the removal of TC from aqueous solutions. The obtained results demonstrated that the adsorption of TC molecules using these MOFs is relatively slow, with the adsorption–desorption equilibrium being reached overnight. This implied that the pore cavities of the MOFs govern the inflow, outflow, and adsorption processes of TC molecules. Further investigation showed that the best Sn-doped MIL-100(Fe), that is MIL-100(Fe,Sn-7.1), behave similarly to MIL-100(Fe) and showed only a slight increase in the adsorption property by about 5% compared to MIL-100(Fe). On the other hand, the best-performing MIL-100(Fe,Ir), that is MIL-100(Fe,Ir-62.3), showed a significant increase in the adsorption property by about 34% under dark conditions compared to MIL-100(Fe). In the photo-Fenton step, however, both of these bimetallic MOFs showed performance comparable to that of MIL-100(Fe). The detailed analysis of the synthesized MOFs revealed that the incorporation of dopants within MIL-100(Fe) frameworks alters the particle size, pore dimensions, and specific surface area of MIL-100(Fe), which in turn affects the adsorption property of this compound. It is shown that, Sn-doping of MIL-100(Fe), that is MIL-100 (Fe,Sn-7.1), increased the surface area from 1536 $m^2\ g^{-1}$ to 1779 $m^2\ g^{-1}$, while no significant changes were observed in the particle size, pore diameter and pore volume of MIL-100(Fe,Sn-7.1) compared to MIL-100(Fe). In contrast, Ir-doping of MIL-100(Fe) resulted in the formation of bimetallic MOFs with a relatively low surface area of 1096 $m^2\ g^{-1}$ for MIL-100(Fe,Ir-62.3), which showed the largest pore diameter of 8.24 nm and pore volume of 2.26 cc g^{-1} when compared with the other MOFs studied in this work. As a consequence, it was clear that the mesoporous nature of MIL-100(Fe,Ir-62.3) is more effective than its surface area value in the TC adsorption process, providing more sites for the adsorption and resulting in the highest removal efficiency of 91% among the studied MOFs. Therefore, it can be concluded that modifying and engineering the pore cavities of MOFs is of prime and fundamental importance for the efficient treatment of wastewater using MOFs.

Data Availability

The data supporting this article have been included as part of the ESI.†

Conflicts of interest

There are no conflicts of interest to declare.

Acknowledgements

We gratefully acknowledge financial support from the Alexander von Humboldt Foundation, the Eva Mayr–Stihl Stiftung in the framework of the Saltus! Project, and funding by the Deutsche Forschungsgemeinschaft (DFG, German Research Foundation) under Germany's Excellence Strategy – EXC-2193/1 – 390951807. We acknowledge support by the Open Access Publication Fund of the University of Freiburg. The authors would like to thank Luis Guillermo Yanez Vazquez for some photochemical measurements and Dr Anneke Georg for ICP-MS measurements. The authors would also like to thank Dr Michael Daub and Dr Thilo Ludwig for XRD measurements.

References

1 D. G. J. Larsson and C.-F. Flach, Antibiotic resistance in the environment, *Nat. Rev. Microbiol.*, 2022, **20**, 257–269.
2 S. A. Kraemer, A. Ramachandran and G. G. Perron, Antibiotic pollution in the environment, *Microorganisms*, 2019, **7**, 180.
3 T. P. Robinson, D. P. Bu, J. Carrique-Mas, E. M. Fèvre, M. Gilbert, D. Grace, S. I. Hay, J. Jiwakanon, M. Kakkar, S. Kariuki, R. Laxminarayan, J. Lubroth, U. Magnusson, P. Thi Ngoc, T. P. van Boeckel and M. E. J. Woolhouse, Antibiotic resistance is the quintessential One Health issue, *Trans. R. Soc. Trop. Med. Hyg.*, 2016, **110**, 377–380.
4 C. Uluseker, K. M. Kaster, K. Thorsen, D. Basiry, S. Shobana, M. Jain, G. Kumar, R. Kommedal and I. Pala-Ozkok, A Review on Occurrence and Spread of Antibiotic Resistance in Wastewaters and in Wastewater Treatment Plants: Mechanisms and Perspectives, *Front. Microbiol.*, 2021, **12**, 717809.
5 J. Wang and R. Zhuan, Degradation of antibiotics by advanced oxidation processes, *Sci. Total Environ.*, 2020, **701**, 135023.
6 B.-E. Channab, M. El Ouardi, O. Ait Layachi, S. E. Marrane, A. El Idrissi, A. BaQais and H. Ait Ahsaine, Recent trends on MIL-Fe metal–organic frameworks: synthesis approaches, structural insights, and applications in organic pollutant adsorption and photocatalytic degradation, *Environ. Sci.: Nano*, 2023, **10**, 2957–2988.
7 H. Chu and C.-C. Wang, MIL-100(Fe)-based functional materials for water decontamination: A state of the art review, *Prog. Nat. Sci.: Mater. Int.*, 2023, **33**, 386–406.
8 F. Ahmad, D. Zhu and J. Sun, Environmental fate of tetracycline antibiotics: degradation pathway mechanisms, challenges, and perspectives, *Environ. Sci. Eur.*, 2021, **33**, 64.
9 M. Zhang, H. Dong, L. Zhao, D. Wang and D. Meng, A review on Fenton process for organic wastewater treatment based on optimization perspective, *Sci. Total Environ.*, 2019, **670**, 110–121.

10 A. M. Chávez, A. Rey, J. López, P. M. Álvarez and F. J. Beltrán, Critical aspects of the stability and catalytic activity of MIL-100(Fe) in different advanced oxidation processes, *Sep. Purif. Technol.*, 2021, **255**, 117660.
11 J. Guo, H. Jia, A. Zhang, Z. Pei, M. Luo, J. Xue, Q. Shen, X. Liu and B. Xu, MIL-100(Fe) with mix-valence coordinatively unsaturated metal site as Fenton-like catalyst for efficiently removing tetracycline hydrochloride, *Sep. Purif. Technol.*, 2021, **262**, 118334.
12 R. Liang, S. Luo, F. Jing, L. Shen, N. Qin and L. Wu, A simple strategy for fabrication of Pd@MIL-100(Fe) nanocomposite as a visible-light-driven photocatalyst for the treatment of pharmaceuticals and personal care products (PPCPs), *Appl. Catal., B*, 2015, **176–177**, 240–248.
13 R. Liang, F. Jing, L. Shen, N. Qin and L. Wu, M@MIL-100(Fe) (M = Au, Pd, Pt) nanocomposites fabricated by a facile photodeposition process, *Nano Res.*, 2015, **8**, 3237–3249.
14 J.-W. Wang, F.-G. Qiu, P. Wang, C. Ge and C.-C. Wang, Boosted bisphenol A and Cr(VI) cleanup over Z-scheme WO_3/MIL-100(Fe) composites under visible light, *J. Cleaner Prod.*, 2021, **279**, 123408.
15 D.-D. Chen, X.-H. Yi, C. Zhao, H. Fu, P. Wang and C.-C. Wang, Polyaniline modified MIL-100(Fe) for enhanced photocatalytic Cr(VI) reduction and tetracycline degradation under white light, *Chemosphere*, 2020, **245**, 125659.
16 M. Zhang, A. Li, Q. Zhou, C. Shuang, W. Zhou and M. Wang, Effect of pore size distribution on tetracycline adsorption using magnetic hypercrosslinked resins, *Microporous Mesoporous Mater.*, 2014, **184**, 105–111.
17 W. Zhang, Y. Shi, C. Li, Q. Zhao and X. Li, Synthesis of bimetallic MOFs MIL-100(Fe-Mn) as an efficient catalyst for selective catalytic Reduction of NOx with NH_3, *Catal. Lett.*, 2016, **146**, 1956–1964.
18 L. Mitchell, P. Williamson, B. Ehrlichová, A. E. Anderson, V. R. Seymour, S. E. Ashbrook, N. Acerbi, L. M. Daniels, R. I. Walton, M. L. Clarke and P. A. Wright, Mixed-Metal MIL-100(Sc,M) (M = Al, Cr, Fe) for Lewis acid catalysis and tandem C–C bond Formation and Alcohol Oxidation, *Chem. – Eur. J.*, 2014, **20**, 17185–17197.
19 X. Zheng, L. Zhang, Z. Fan, Y. Cao, L. Shen, C. Au and L. Jiang, Enhanced catalytic activity over MIL-100(Fe) with coordinatively unsaturated Fe2+/Fe3+ sites for selective oxidation of H_2S to sulfur, *Chem. Eng. J.*, 2019, **374**, 793–801.
20 M. Giménez-Marqués, A. Santiago-Portillo, S. Navalón, M. Álvaro, V. Briois, F. Nouar, H. Garcia and C. Serre, Exploring the catalytic performance of a series of bimetallic MIL-100(Fe, Ni) MOFs, *J. Mater. Chem. A*, 2019, **7**, 20285–20292.
21 T. Steenhaut, S. Hermans and Y. Filinchuk, Green synthesis of a large series of bimetallic MIL-100(Fe,M) MOFs, *New J. Chem.*, 2020, **44**, 3847–3855.
22 J. H. Scofield, Hartree-Slater subshell photoionization cross-sections at 1254 and 1487 eV, *J. Electron Spectrosc. Relat. Phenom.*, 1976, **8**, 129–137.
23 Z. Wang, H. Wang, P. Wang, X. Liu, X. Lei, R. Guo, J. You and H. Zhang, Application of MOFs driven by various energy sources for degradation the organic pollutants in water: A review, *Coord. Chem. Rev.*, 2024, **499**, 215506.
24 C. Du, Y. Zhang, Z. Zhang, L. Zhou, G. Yu, X. Wen, T. Chi, G. Wang, Y. Su, F. Deng, Y. Lv and H. Zhu, Fe-based metal organic frameworks (Fe-MOFs) for organic pollutants removal via photo-Fenton: A review, *Chem. Eng. J.*, 2022, **431**, 133932.
25 Q. Wu, M. S. Siddique, Y. Guo, M. Wu, Y. Yang and H. Yang, Low-crystalline bimetallic metal-organic frameworks as an excellent platform for photo-Fenton degradation of organic contaminants: Intensified synergism between hetero-metal nodes, *Appl. Catal., B*, 2021, **286**, 119950.
26 S. Wang, F. Meng, X. Sun, M. Bao, J. Ren, S. Yu, Z. Zhang, J. Ke and L. Zeng, Bimetallic Fe/In metal-organic frameworks boosting charge transfer for enhancing pollutant degradation in wastewater, *Appl. Surf. Sci.*, 2020, **528**, 147053.
27 T. K. Vo, Y.-S. Bae, B.-J. Chang, S.-Y. Moon, J.-H. Kim and J. Kim, Highly CO selective Cu(I)-doped MIL-100(Fe) adsorbent with high CO/CO_2 selectivity due to π complexation: Effects of Cu(I) loading and activation temperature, *Microporous Mesoporous Mater.*, 2019, **274**, 17–24.
28 A. Mancuso, O. Sacco, V. Vaiano, B. Bonelli, S. Esposito, F. S. Freyria, N. Blangetti and D. Sannino, Visible Light-Driven Photocatalytic Activity and Kinetics of Fe-Doped TiO_2 Prepared by a Three-Block Copolymer Templating Approach, *Materials*, 2021, **14**, 3105.
29 M. Fouad, M. Gar Alalm, H. K. El-Etriby, D. C. Boffito, S. Ookawara, T. Ohno and M. Fujii, Visible-light-driven photocatalytic disinfection of raw surface waters (300–5000 CFU/mL) using reusable coated $Ru/WO_3/ZrO_2$, *J. Hazard. Mater.*, 2021, **402**, 123514.
30 M. Cheng, C. Lai, Y. Liu, G. Zeng, D. Huang, C. Zhang, L. Qin, L. Hu, C. Zhou and W. Xiong, Metal-organic frameworks for highly efficient heterogeneous Fenton-like catalysis, *Coord. Chem. Rev.*, 2018, **368**, 80–92.
31 Y. Fang, Z. Yang, H. Li and X. Liu, MIL-100(Fe) and its derivatives, *Environ. Sci. Pollut. Res.*, 2020, **27**, 4703–4724.
32 X. Li, W. Guo, Z. Liu, R. Wang and H. Liu, Fe-based MOFs for efficient adsorption and degradation of acid orange 7 in aqueous solution via persulfate activation, *Appl. Surf. Sci.*, 2016, **369**, 130–136.
33 W. Li, J. Cao, W. Xiong, Z. Yang, S. Sun, M. Jia and Z. Xu, In-situ growing of metal-organic frameworks on three-dimensional iron network as an efficient adsorbent for antibiotics removal, *Chem. Eng. J.*, 2020, **392**, 124844.
34 Z. Mohammadifard, R. Saboori, N. S. Mirbagheri and S. Sabbaghi, Heterogeneous photo-Fenton degradation of formaldehyde using MIL-100(Fe) under visible light irradiation, *Environ. Pollut.*, 2019, **251**, 783–791.
35 B. van de Voorde, M. Boulhout, F. Vermoortele, P. Horcajada, D. Cunha, J. S. Lee, J.-S. Chang, E. Gibson, M. Daturi, J.-C. Lavalley, A. Vimont, I. Beurroies and D. E. de Vos, N/S-Heterocyclic contaminant removal from fuels by the mesoporous metal–organic framework MIL-100, *J. Am. Chem. Soc.*, 2013, **135**, 9849–9856.

36 K. Guesh, C. A. D. Caiuby, Á. Mayoral, M. Díaz-García, I. Díaz and M. Sanchez-Sanchez, Sustainable preparation of MIL-100(Fe) and its photocatalytic behavior in the degradation of Methyl Orange in Water, *Cryst. Growth Des.*, 2017, **17**, 1806–1813.

37 J. Tauc and A. Menth, States in the Gap, *J. Non-Cryst. Solids*, 1972, **8–10**, 569–585.

38 K. S. W. Sing, Reporting physisorption data for gas/solid systems with special reference to the determination of surface area and porosity (Provisional), *Pure Appl. Chem.*, 1982, **54**, 2201–2218.

39 D. Wang, F. Jia, H. Wang, F. Chen, Y. Fang, W. Dong, G. Zeng, X. Li, Q. Yang and X. Yuan, Simultaneously efficient adsorption and photocatalytic degradation of tetracycline by Fe-based MOFs, *J. Colloid Interface Sci.*, 2018, **519**, 273–284.

40 S. Nayab, V. Trouillet, H. Gliemann, P. G. Weidler, I. Azeem, S. R. Tariq, A. S. Goldmann, C. Barner-Kowollik and B. Yameen, Reversible Diels–Alder and Michael Addition Reactions Enable the Facile Postsynthetic Modification of Metal–Organic Frameworks, *Inorg. Chem.*, 2021, **60**, 4397–4409.

41 M. C. Biesinger, B. P. Payne, A. P. Grosvenor, L. W. Lau, A. R. Gerson and R. S. Smart, Resolving surface chemical states in XPS analysis of first row transition metals, oxides and hydroxides: Cr, Mn, Fe, Co and Ni, *Appl. Surf. Sci.*, 2011, **257**, 2717–2730.

42 A. Wieczorek, H. Lai, J. Pious, F. Fu and S. Siol, Resolving Oxidation States and X–site Composition of Sn Perovskites through Auger Parameter Analysis in XPS, *Adv. Mater. Interfaces*, 2022, **10**, 2201828.

43 V. Pfeifer, T. E. Jones, J. J. Velasco Vélez, C. Massué, R. Arrigo, D. Teschner, F. Girgsdies, M. Scherzer, M. T. Greiner, J. Allan, M. Hashagen, G. Weinberg, S. Piccinin, M. Hävecker, A. Knop-Gericke and R. Schlögl, The electronic structure of iridium and its oxides, *Surf. Interface Anal.*, 2016, **48**, 261–273.

44 A. C. Martins, O. Pezoti, A. L. Cazetta, K. C. Bedin, D. A. Yamazaki, G. F. Bandoch, T. Asefa, J. V. Visentainer and V. C. Almeida, Removal of tetracycline by NaOH-activated carbon produced from macadamia nut shells, *Chem. Eng. J.*, 2015, **260**, 291–299.

45 G. Lyngsie, L. Krumina, A. Tunlid and P. Persson, Generation of hydroxyl radicals from reactions between a dimethoxyhydroquinone and iron oxide nanoparticles, *Sci. Rep.*, 2018, **8**, 10834.

46 M. Li, Y. Ma, J. Jiang, T. Li, C. Zhang, Z. Han and S. Dong, Enhanced photo-Fenton degradation of tetracycline hydrochloride by 2, 5-dioxido-1, 4-benzenedicarboxylate-functionalized MIL-100(Fe), *Environ. Res.*, 2022, **212**, 113399.

47 A. J. Bard and L. R. Faulkner, *Electrochemical Methods: Fundamentals and Applications*, Wiley, New York, 2001.

48 P. M. Wood, The potential diagram for oxygen at pH 7, *Biochem. J.*, 1988, **253**, 287–289.

49 D. A. Armstrong, R. E. Huie, W. H. Koppenol, S. V. Lymar, G. Merényi, P. Neta, B. Ruscic, D. M. Stanbury, S. Steenken and P. Wardman, Standard electrode potentials involving radicals in aqueous solution: inorganic radicals (IUPAC Technical Report), *Pure Appl. Chem.*, 2015, **87**, 1139–1150.

50 H. U. Rasheed, X. Lv, S. Zhang, W. Wei, N. Ullah and J. Xie, Ternary MIL-100(Fe)@Fe_3O_4/CA magnetic nanophotocatalysts (MNPCs): Magnetically separable and Fenton-like degradation of tetracycline hydrochloride, *Adv. Powder Technol.*, 2018, **29**, 3305–3314.